ACS NANO

www.acsnano.org

ARTICLE

Quantitative Mid-infrared Photoluminescence Characterization of Black Phosphorus–Arsenic Alloys

Shu Wang, Naoki Higashitarumizu, Bengisu Sari, Mary C. Scott, and Ali Javey*

Cite This: *ACS Nano* 2024, 18, 5907–5914

Read Online

ACCESS | Metrics & More | Article Recommendations | Supporting Information

ABSTRACT: **Black phosphorus (bP) is a promising material for mid-infrared (mid-IR) optoelectronic applications, exhibiting high performance light emission and detection. Alloying bP with arsenic extends its operation toward longer wavelengths from 3.7 μm (bP) to 5 μm (bP_3As_7), which is of great practical interest. Quantitative optical characterizations are performed to establish black phosphorus–arsenic (bPAs) alloys optoelectronic quality. Anisotropic optical constants (refractive index, extinction coefficient, and absorption coefficient) of bPAs alloys from near-infrared to mid-IR (0.2–0.9 eV) are extracted with reflection measurements, which helps optical device design. Quantitative photoluminescence (PL) of bPAs alloys with different As concentrations are measured from room temperature to 77 K. PL quantum yield measurements reveal a 2 orders of magnitude decrease in radiative efficiency with increasing As concentration. An optical cavity is designed for bP_3As_7, which allows for up to an order of magnitude enhancement in the quantum yield due to the Purcell effect. Our comprehensive optical characterization provides the foundation for high performance mid-IR optical device design using bPAs alloys.**

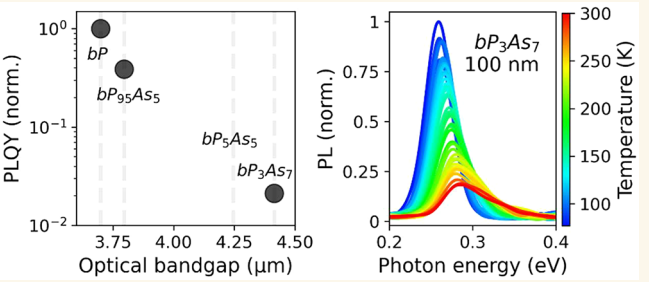

KEYWORDS: *Phosphorus–arsenic alloys, photoluminescence quantum yield, mid-infrared, anisotropic, optical constant, positive band gap temperature coefficient, optical cavity*

Mid-infrared (mid-IR) optoelectronics have been of considerable importance for applications in sensing, imaging, and communication. However, mid-IR light sources suffer from high power consumption (e.g., quantum and interband cascade lasers) and/or low radiative efficiency (e.g., light emitting diodes). This performance limitation is partly due to the enhanced Auger recombination rate as the semiconductor band gap is reduced to mid-IR.[1] Black phosphorus (bP), with a bulk direct energy band gap of 0.33 eV (3.7 μm), has shown great promise for high-performance mid-IR photodetectors and emitters.[2] Notably, as compared to conventional III–V and II–VI semiconductors with similar band gaps, bP exhibits a lower Auger recombination rate[3] due to its more symmetric electron/hole effective mass.[1,4,5] To further the applications of black phosphorus toward longer wavelengths, various techniques have been demonstrated, including applying compressive strain,[6,7] tuning the electric field,[8] applying pressure,[9] and alloying with other group V elements such as arsenic.[10−13] Alloying is promising, as it can be directly incorporated into existing device designs.

In the past few years, various studies have demonstrated mid-IR photodetectors (phototransistor and photodiode, with high responsivity) with black phosphorus arsenic (bPAs) alloys,[10−13] while electroluminescence of a bPAs heterostructure[14] and simulated emission of bPAs in a cavity at 3.4–4.7 μm[15] have been reported recently. Despite considerable research highlighting bPAs mid-IR optoelectronic device potential,[11,12,14,16] detailed quantitative optical characterization as a function of As concentration is still lacking. Such data are needed for optimal design of bPAs optoelectronic devices while projecting their performance limits.

In this paper, we perform comprehensive bPAs alloy photoemission and optical absorption measurements using customized Fourier-transform infrared spectroscopy (FTIR)

Received: December 21, 2023
Revised: January 26, 2024
Accepted: January 30, 2024
Published: February 9, 2024

https://doi.org/10.1021/acsnano.3c12927
ACS Nano 2024, 18, 5907–5914

for As concentrations from 0% to 70%. The refractive index (n) and extinction coefficient (k) of bPAs alloys from 0.2 to 0.9 eV are extracted using thickness dependent reflection measurement. Anisotropic absorption of bPAs is demonstrated with a polarized reflection study. Photoluminescence quantum yields (PLQYs) for bPAs alloys are measured. Using the optical constants measured in this work, an optimal optical cavity is designed with increased Purcell factor, demonstrating an order of magnitude enhancement in PLQY. Temperature dependent PL from 77 K to room temperature for bPAs alloys is studied. Our results can be used to design high performance mid-IR optoelectronic devices in 3−5 μm with bPAs alloys.

RESULTS AND DISCUSSION

BPAs alloy is mechanically exfoliated in a nitrogen glovebox and measured in a vacuum chamber, with HgCdTe (MCT) detector in an FTIR set up with lock-in detection (see Methods).[6,17,18] BPAs alloys with thicknesses ranging from 20 nm to 1 μm are measured. As shown in Figure 1, the bPAs PL

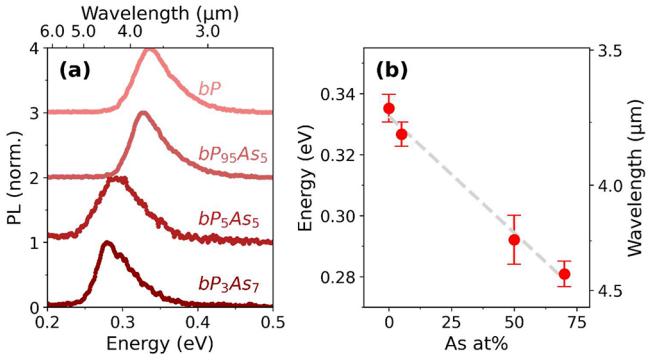

Figure 1. Photoluminescence of bPAs alloys. (a) Normalized photoluminescence spectra of bP, $bP_{95}As_5$, bP_5As_5, and bP_3As_7 at room temperature. (b) Optical band gap extracted from photoluminescence spectra in (a). Linear fit is shown. Error bars show standard deviations calculated from extracted peak positions of multiple (~20) measurements at each alloy composition.

band gap changes from 0.33 eV for bP to 0.28 eV for bP_3As_7, which corresponds to a wavelength change from 3.7 to 4.4 μm. No significant difference in the PL spectrum is observed for the measured thickness range (Figure S4), as the explored thickness is large enough to minimize quantum confinement effects. The choice of relatively thick samples (>20 nm, where a blue-shift of the band gap due to quantum effect is negligible) is in consideration of its application in mid-IR, where the performance of both light emission and detection devices still has much to improve. The upper thickness limit of samples used in this study (1 μm) is determined by the measured absorption depth, as detailed below. No significant PL spectrum change is observed in the incident light power range, except for a small increase of the spectrum full-width-at-half-maximum (fwhm) with increased power due to local heating (Figure S4). A small absorption dip is observed for the bP_3As_7 PL spectrum at 0.29 eV (also evident bP_5As_5), due to the atmospheric carbon dioxide (~500 ppm) absorption, indicating high sensitivity for bPAs in application of environmental sensing.[6,19]

The composition and material quality used in this study is characterized by energy dispersive X-ray spectroscopy (EDS), Raman spectrum, and transmission electron microscope (TEM). Scanning electron microscope EDS characterization reveals the alloy compositions of each sample (bP, $bP_{95}As_5$, bP_5As_5 and bP_3As_7, see Figures 2 and S1). The polarization

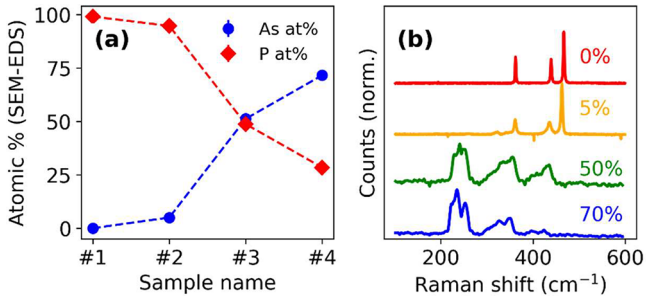

Figure 2. Material characterization (Raman and EDS) of samples studied in this paper. (a) Energy-dispersive X-ray spectroscopy of bPAs alloys showing their atomic composition. Sample numbers 1−4 correspond to bP, $bP_{95}As_5$, bP_5As_5, and bP_3As_7, respectively, used in this paper. (b) Unpolarized Raman spectra for bP, $bP_{95}As_5$, bP_5As_5, and bP_3As_7.

resolved Raman spectra for different bPAs alloys are measured, as shown in Figure 2 and S2. Feature Raman peak positions for bP (362, 440, and 467 cm^{-1}) and As (between 210 and 260 cm^{-1}), along with the gradual shift and broadening of peak position due to alloying are evident, which shows the compositional difference for the samples used in this paper.[20,21] Clear evidence of polarization dependence can be observed for the material from the Raman spectra, especially for bP and 5 atom % As alloy (more than 1 order intensity difference for the A_g^1 mode; see Figure S2). High-resolution transmission electron microscopy (HRTEM) images for bP_3As_7 and $bP_{95}As_5$ show the crystal quality of the samples used (Figure 3). Selected area electron diffraction (SAED) patterns of bP_3As_7 and $bP_{95}As_5$ along the z axis demonstrate

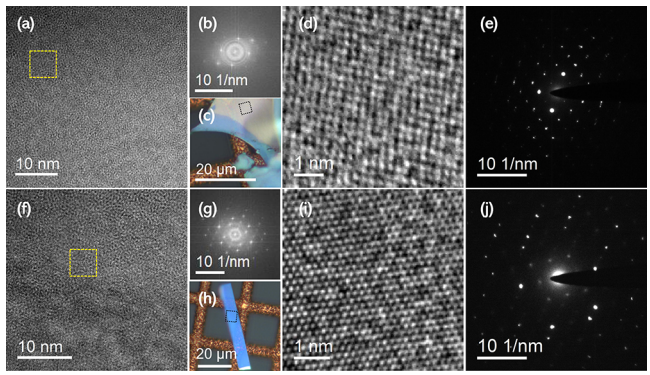

Figure 3. TEM characterization bPAs alloys. (a−e) bP_3As_7 and (f−j) $bP_{95}As_5$. (a) HRTEM image of bP_3As_7 alloy. (b) Fast Fourier transform of image (a). (c) Optical microscope image of the sample used for TEM imaging in (a−e), where the imaged area is marked in dashed black square. (d) Magnified HRTEM image of sample area marked in yellow dashed square in (a). (e) Parallel beam diffraction pattern of sample shown in (c) with camera length 160 mm and 300 kV. (f) HRTEM image of $bP_{95}As_5$ alloy. (g) Fast Fourier transform of image (f). (h) Optical microscope image of the sample used for TEM imaging in (f−j), where the imaged area is marked in dashed black square. (i) Magnified HRTEM image of sample area marked in yellow dashed square in (f). (j) Parallel beam diffraction pattern of sample shown in (h) with camera length 160 mm and 300 kV.

https://doi.org/10.1021/acsnano.3c12927
ACS Nano 2024, 18, 5907−5914

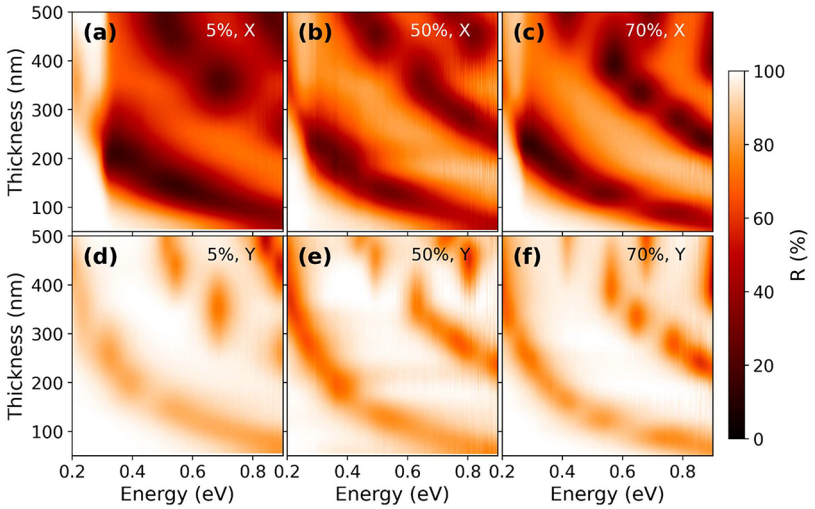

Figure 4. Anisotropic reflection of bPAs alloys with different thicknesses on gold. (a–c) Armchair (*X*) direction reflection of $bP_{95}As_5$, bP_5As_5, and bP_3As_7 on gold. (d–f) Zigzag (*Y*) direction reflection of $bP_{95}As_5$, bP_5As_5, and bP_3As_7 on gold.

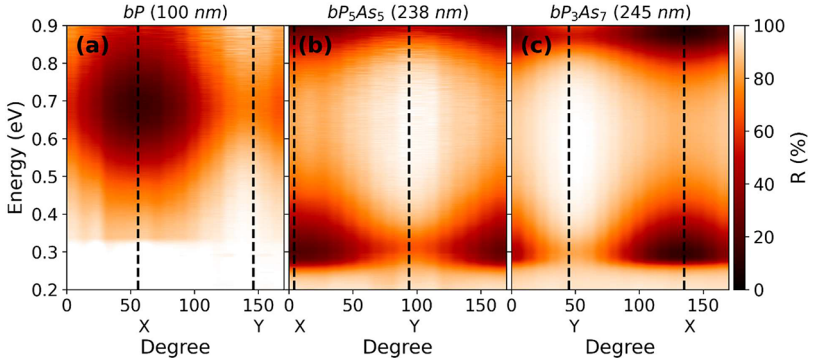

Figure 5. Anisotropic reflection of bPAs (alloy) on gold. (a) bP reflection on gold, with light polarization from 0° to 170°. (b) bP_5As_5 reflection on gold, with light polarization from 0° to 170°. (c) bP_3As_7 reflection on gold, with light polarization from 0° to 170°. Armchair (*X*) and zigzag (*Y*) directions determined from minimum and maximum reflection, as shown in each subplot, and used for determining *X* and *Y* directions for Figure 4.

the crystallinity of the samples, with the extracted lattice constants (a = 3.3 Å, c = 4.4 Å for $bP_{95}As_5$, a = 3.57 Å, c = 4.2 Å for bP_3As_7) and the diffraction patterns matching those of orthorhombic bPAs alloys (Figures 3 and S5).[22,23] The lattice constant for $bP_{95}As_5$ is similar to that of bP. Interestingly, for bP_3As_7, the armchair direction lattice constant is larger than the reported value for bP and black arsenic (bAs), and the zigzag direction lattice constant is smaller than those of bP and bAs, probably due to the atom size difference of P and As.[24,25]

Besides band gap and material quality, the optical constants (refractive index, n, and extinction coefficient, k) of a material are important for optical device design. Here, the reflection spectra of bPAs alloys are measured as a function of material thickness. Exfoliated bPAs alloys with thicknesses from 50 to 500 nm are used for each composition (10–20 evenly spaced thicknesses). With thin film transfer matrix theory, (n, k) values can be extracted from the measured reflection spectra.[26,27] Figure 4 shows the measured reflection spectra for three compositions of bPAs alloys on the Au substrate as a function of sample thickness. The clear effect of thin-film interference due to different n, k, and thickness values of the layers is observed. Light absorption in the *X* direction is significantly higher than that in the *Y* direction, as evidenced by the reduced reflection. The detailed anisotropic features of bPAs alloys are demonstrated in Figure 5, with measured reflection spectra of individual exfoliated flakes using polarized light ranging from 0° to 170°. From the measured reflection, the *X* direction (armchair) is denoted as the direction with maximum absorption of light, while the *Y* direction (zigzag) is denoted as the direction with minimum absorption of light (thus maximum reflection), which is how the *X* and *Y* directions in Figure 4 are determined. Applying thin-film transfer matrix method (details in Methods section),[26] fitted (n, k) values from 0.2 to 0.9 eV from data measured in Figure 4 are shown in Figure 6. The absorption coefficient, α, is calculated from the extinction coefficient and wavelength ($\alpha = \frac{4\pi k}{\lambda}$, where λ is wavelength). Absorption edges, which correspond to energy band edges, for the alloys can be observed in the *X* direction k (or α) values. The energy band gaps extracted from fitted (n, k) values are 0.32 eV for bP, 0.31 eV for $bP_{95}As_5$, 0.26 eV for bP_5As_5, and 0.255 eV for bP_3As_7 (Figure 7), which is consistent with extracted band gaps from PL measurements. The absorption coefficient is $1-2 \times 10^4$ cm^{-1} for 0.4–0.9 eV in the *X* direction, which indicates the absorption depth is around 500 nm to 1 μm.

Photoluminescence quantum yield is a key merit for characterizing the radiative to nonradiative recombination rate of an emission material.[28] We measured the PLQY for the

https://doi.org/10.1021/acsnano.3c12927
ACS Nano 2024, 18, 5907–5914

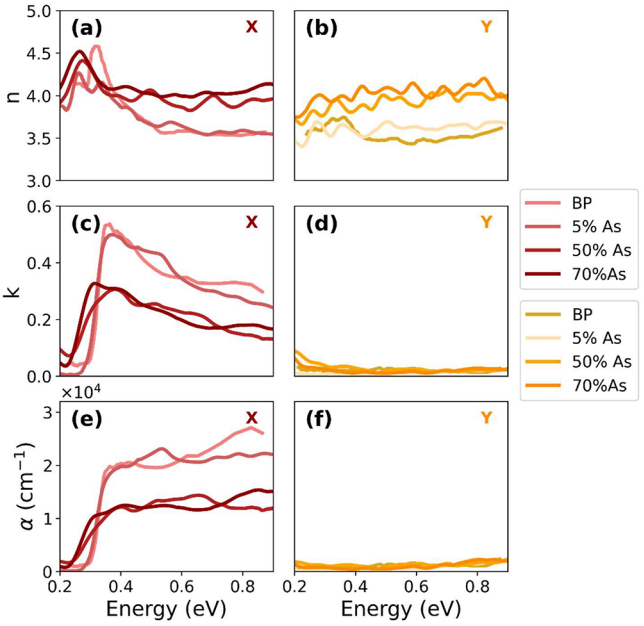

Figure 6. Optical constants of bPAs alloys. Data from fitting polarized reflection measurements of bPAs alloys with different thicknesses shown in Figure 4. Fitting adopts transfer matrix method. (a, c, e) Armchair (X) direction optical constants (n, k, α) for bP, $bP_{95}As_5$, bP_5As_5, and bP_3As_7. (b, d, f) Zigzag (Y) direction optical constants (n, k, α) for bP, $bP_{95}As_5$, bP_5As_5, and bP_3As_7. BP data adopted from ref 27.

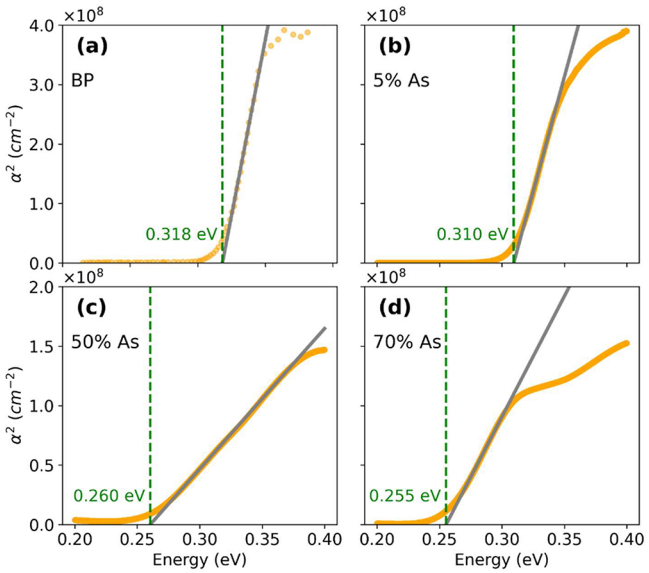

Figure 7. BPAs (alloy) band gap estimation from extracted optical constant. (a) Band gap estimation for bP. (b) Band gap estimation for $bP_{95}As_5$. (c) Band gap estimation for bP_5As_5. (d) Band gap estimation for bP_3As_7. BP data adopted ref 27.

bPAs alloys as shown in Figure 8.[6] Laser polarization is aligned to the X direction (maximum absorption) with ±30° accuracy, as in the crystal orientation where light absorption is weak, the PL signal is weak, and measurement error is large. With 5 atom % As incorporation, PLQY is still comparable to bP (decrease ~ 3 times); when the As concentration increases to 70%, a 2 orders of magnitude decrease of PLQY is observed. A general trend of decreasing PLQY with an increasing generation rate is observed, which could be the result of stronger Auger recombination at higher carrier concentrations. A decrease of PLQY with decreasing thickness is observed for $bP_{95}As_5$, which can be attributed to a higher surface to volume ratio and thus an increasing effect of nonradiative surface recombination.

Stronger Auger recombination due to a smaller band gap contributes to the lowering of PLQY when As concentration increases in bPAs alloys. The ratio of Auger coefficient to radiative coefficient changes exponentially with band gap: $\frac{\tau_{Auger}}{\tau_{rad}} \propto \exp\left[\frac{m_c}{m_c + m_h} \cdot \frac{E_g}{k_B T}\right]$, where τ_{Auger} is Auger recombination lifetime, τ_{rad} is radiative recombination lifetime, m_c and m_h are effective masses for electron and hole, E_g is band gap, and $k_B T$ is thermal energy.[1,6] Besides stronger Auger recombination for bPAs alloys with high As concentration, the crystal quality of the material contributes to the lowering of the PLQY. Note that the typical efficiency for 4 μm light emitting diode is 10^{-3} (for epitaxial quantum wells or HgTe colloidal quantum dots).[29−31] For practical applications of bPAs alloys for light emission, designs to enhance radiative recombination are needed, including low temperature operation or the incorporation of an optical cavity as reported below.

Nonradiative recombinations are typically suppressed at low temperatures, where phonon assisted processes are suppressed due to lower available thermal energies. The energy band gap of a semiconductor commonly increases with decreasing temperature,[32] while some materials including bP show positive band gap temperature coefficient.[33−35] To study the effect of temperature on bPAs alloy luminescence properties, we measure temperature dependent PL for bP, $bP_{95}As_5$, bP_5As_5, and bP_3As_7. All samples are exfoliated in a nitrogen environment, before transferring to a vacuum chamber and cool down to 77 K. Subsequent PL spectra are measured while the vacuum chamber warms up toward room temperature. PL peak position at 77 K changes from 0.31 eV for bP to 0.25 eV for bP_3As_7 (Figures 9 and S6). Contrary to that observed at room temperature, the lower energy side of the spectrum is broader (Figure S6, Figure 1), which may be attributed to band tailing. PL spectra as a function of temperature are shown in Figure 9, with extracted peak positions and spectra fwhms (Figure 10). Positive temperature coefficient is observed for all compositions. Small decreasing trend for the band gap temperature coefficient is observed when the As concentration increases (1.6×10^{-4} eV/K for bP, to 1.2×10^{-4} eV/K for bP_3As_7). The PL spectra are sharper at lower temperatures (fwhm changes from 40 to 65 meV). As shown in Figure 10, a clear enhancement of radiative recombination at 77 K is observed. The integrated counts from the PL spectra (which is proportional to radiative quantum efficiency) show a gradual increase when the temperature decreases, reaching 2x enhancement at 77 K.

The spontaneous radiative emission rate of a material can be influenced by its dielectric environment. The Purcell factor quantitatively describes the effect of the cavity on the radiative emission rate. With a designed cavity, the Purcell factor changes by orders of magnitude, significantly extending the application ability of an optical material.[15,17,36] Due to its interlayer van der Waals bonding nature, bPAs alloys can be readily incorporated into designed optical cavities without sacrificing its radiative emission rate.[17,18] Here, we fabricate an optical cavity with increased Purcell factor (~20) compared to the Si wafer substrate used for the rest of the paper. As illustrated in Figure 11, the cavity for bP_3As_7 consists of a bottom Au reflector and top ITO half-reflector, with Al_2O_3 and

https://doi.org/10.1021/acsnano.3c12927
ACS Nano 2024, 18, 5907−5914

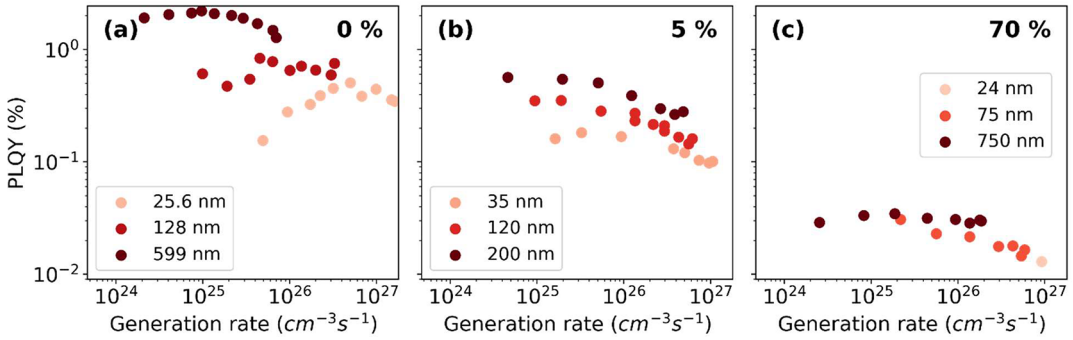

Figure 8. Photoluminescence quantum yield of bPAs alloys. (a) PLQY of bP (data adapted from ref 17). Different colors represent different thicknesses, where light red is 25.6 nm, red is 128 nm, and dark red is 599 nm. (b) PLQY of $bP_{95}As_5$. The colors of the scatter plot represent different thicknesses, where light red is 35 nm, red is 120 nm, and dark red is 200 nm. (c) PLQY of bP_3As_7. Specimens of different thicknesses are represented with color, where light red is 24 nm, red is 75 nm, and dark red is 750 nm.

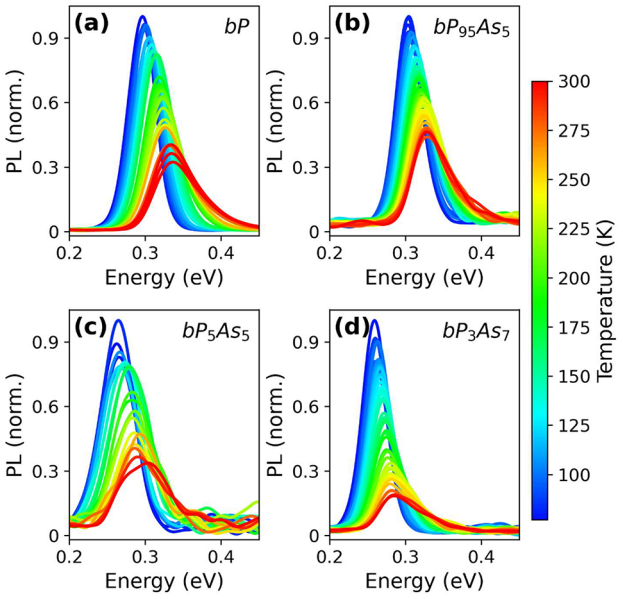

Figure 9. Temperature dependent photoluminescence spectra of bPAs alloys. (a–d) PL spectra from 77 K to room temperature for bP, $bP_{95}As_5$, bP_5As_5, and bP_3As_7. Thicknesses are 500 nm for bP, 94.6 nm for $bP_{95}As_5$, 250 nm for bP_5As_5, and 100 nm for bP_3As_7.

h-BN as spacers. The measured PL spectrum of bP_3As_7 inside the cavity is consistent with that measured on Si wafers. A small blue-shift and broadening of PL is observed, which results from local heating due to enhanced (2x) absorption and high pump power. The PLQY with cavity is significantly enhanced, reaching 0.5%, which is comparable to bP of similar thickness. The effect can also be understood by constructive interference of PL from bPAs. The extreme circumstance of this cavity enhancement will be lasing,[15,36] which requires more dedicated device fabrication techniques and thus beyond the scope of this work. Nevertheless, the demonstration of the enhanced luminescence yield of bPAs alloy shows its promise for high performance mid-IR emission devices, especially when considering layered materials like bPAs alloy do not have as much constraint for lattice matching as traditional III–V and II–VI semiconductors.

CONCLUSIONS

To summarize, we report optical and optoelectronic properties of bPAs alloys for mid-IR light emission and detection applications. BPAs alloys room temperature luminescence wavelength extend to 4.4 μm with bP_3As_7. A significant decrease in radiative emission efficiency is observed for high As concentration bPAs alloys, which can be compromised by incorporating an optical cavity. Anisotropic optical constants measured for bPAs alloys from 0.2 to 0.9 eV provide the building block for optical device design. Positive temperature dependence of the optical band gap indicates a negative pressure coefficient and/or nontraditional electron–phonon coupling in this layered alloy system. Further development of practical mid-IR optoelectronics with bPAs alloys will benefit from cavity designs (for increased radiative recombination), surface treatments or packaging techniques (for long operation lifetime), as well as large-scale high-quality synthesis of the bPAs material.

METHODS

Materials. Black phosphorus–arsenic alloys are purchased from hQ graphene (chemical vapor transport synthesis with Tin as catalyst), stored in a nitrogen box, and used as received. Samples are exfoliated with Scotch tape, transferred to PDMS, and finally transferred to target substrates. For reflection measurements, substrates are Au, which is 5 nm Ti + 80 nm Au evaporated on clean Si wafers. For the cavity, the substrate is evaporated 100 nm Au + sputtered 180 nm Al_2O_3 on a clean Si wafer. For all other PL measurements, the substrate is a Si wafer with 50 nm SiO_2.

Material Characterization. Energy dispersive X-ray spectroscopy is measured with FEI Quanta scanning electron microscopy at The California Institute for Quantitative Biosciences at UC Berkeley. Samples used in this study show a small variation (3%), especially for bP_5As_5 and bP_3As_7 alloys (Figure S1). Along with the 1% error inherent in EDS analysis, the composition should be interpreted with error in mind.

The Raman spectrum is measured with a commercial Raman (Horiba Labram HR evolution) with a 473 nm laser focused on samples by 100× objective at UC Berkeley.

Transmission electron microscope characterization (high-resolution transmission electron microscopy and selected area electron diffraction) is measured with a FEI Titan 60–300 microscope with acceleration voltage 300 kV at the National Center for Electron Microscopy at Lawrence Berkeley National Laboratory. Samples for TEM are prepared in a nitrogen glovebox. First exfoliate source material with Scotch tape, then transfer flakes from Scotch tape to PDMS, then transfer flakes from PDMS to clean Si wafer (with 50 nm oxide), then add 5 μL of ethanol alcohol on the TEM grid (G100HS, Copper, Tedpella) placed near the target flake on the Si wafer, then finally anneal at 90 °C and check with optical microscope.

FTIR PL Measurement. Photoluminescence measurement with customized set up using FTIR + lock-in amplifier has been reported

https://doi.org/10.1021/acsnano.3c12927
ACS Nano 2024, 18, 5907–5914

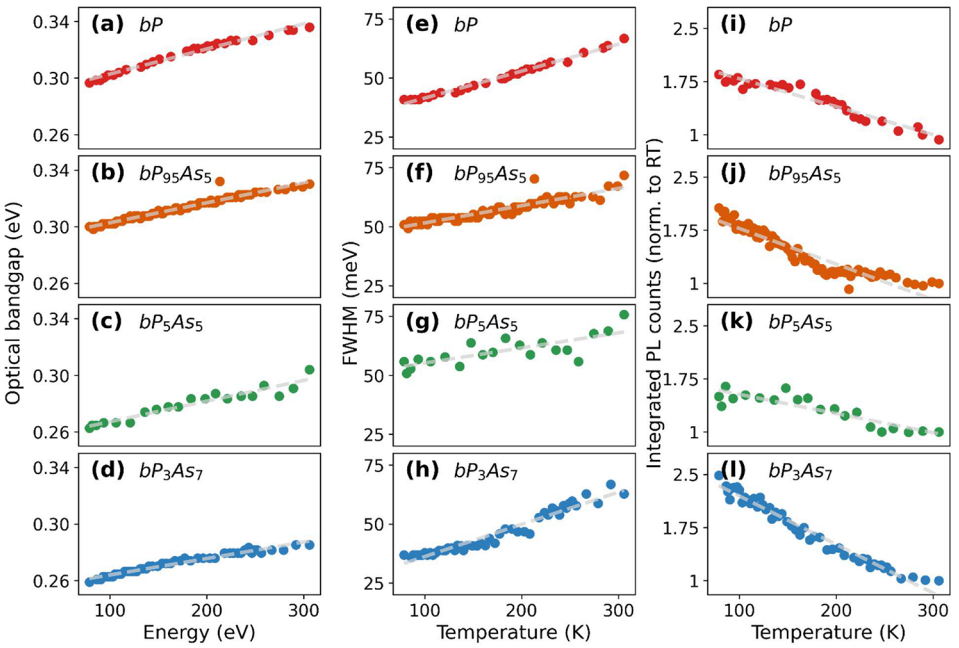

Figure 10. Temperature dependent photoluminescence data of bPAs alloys. (a–d) Optical band gap extracted from PL spectra in Figure 9 from 77 K to room temperature for bP, $bP_{95}As_5$, bP_5As_5, and bP_3As_7. (e–h) Full width at half-maximum (fwhm) extracted from PL spectra in Figure 9 from 77 K to room temperature for bP, $bP_{95}As_5$, bP_5As_5, and bP_3As_7. (i–l). Integrated counts from PL spectra in Figure 9 from 77 K to room temperature for bP, $bP_{95}As_5$, bP_5As_5, and bP_3As_7. Counts normalized to each room temperature counts. Linear fitting is shown for each subfigure.

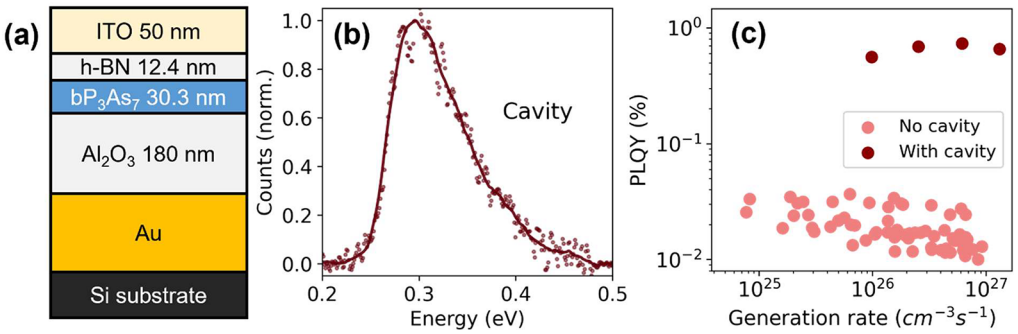

Figure 11. Optical cavity design for high quantum yield emitter with bP_3As_7. (a) Cavity structure. (b) Normalized photoluminescence spectrum of bP_3As_7 in the cavity. Note the spectrum is slightly blue-shifted due to local heating. (c) Estimated PLQY for the cavity (30.3 nm), as compared to samples directly exfoliated on Si wafers (multiple samples with thicknesses 20 nm to 1 μm).

previously.[6,17,18] Samples are exfoliated in a nitrogen glovebox and quickly transferred to the vacuum chamber. Sample inside a vacuum chamber (CaF_2 window, $<1 \times 10^{-5}$ Torr) is excited with modulated 638 nm laser, with emission collected by an FTIR (Thermo Scientific, Nicolet is50) with a 15x reflective objective lens, where PL signal (not thermal background) is extracted using lock-in detection technique modulated at 5k Hz. Polarization is aligned with rotating the sample perpendicular to the laser until maximum PL intensity. For quantitative PL study, set up collection efficiency is calibrated using 4 μm QCL laser with Spectralon placed at the sample position, while thin film absorption/emission properties are simulated with finite-difference time-domain method (Ansys Lumerical).

FTIR Polarized Reflection Measurement. FTIR left microscope is used for microreflection measurement. Built-in IR source (1000 K thermal source) is directed toward a 32× reflective objective focused on either the sample or the Au reflection reference. CaF_2 holographic wire grid polarizer (Thorlabs) is used for creating a polarized light source from the IR source. BPAs alloy samples are measured in air within 4 h of exfoliation to minimize the effect of ambient conditions on their surfaces.

Thin Film Transfer Matrix Method. Equation for analyzing multilayer systems adopted from reference, which considers multi-reflection and light interference.[26] Normal incidence on a perfect thin-film stack is assumed. The method is described as follows:

The amplitude reflection r of a semi-infinite film stack is

$$r = \frac{n_m E_m - H_m}{n_m E_m + H_m}$$

where E_m and H_m are electric vector and magnetic vector and n_m is the refractive index of layer m:

$$\begin{pmatrix} E_m \\ H_m \end{pmatrix} = M \begin{pmatrix} 1 \\ n_s \end{pmatrix}$$

M is a product matrix:

$$M = M_L M_{L-1} \ldots M_1$$

https://doi.org/10.1021/acsnano.3c12927
ACS Nano 2024, 18, 5907–5914

$$M_j = \begin{pmatrix} \cos\delta_j & \frac{i}{n_j}\sin\delta_j \\ in_j\sin\delta_j & \cos\delta_j \end{pmatrix}$$

with $\delta_j = \frac{2\pi}{\lambda}(n_j d_j)$, λ is light wavelength, d_j is thickness of layer j.The intensity reflectance for thin film stack of air, bPAs and Au is

$$R = |r|^2 = \left| \frac{\cos\delta_j - \cos\delta_j \cdot n_{Au} + i\frac{n_{Au}}{\eta_{bPAs}}\sin\delta_j - i\eta_{bPAs}\sin\delta_j}{\cos\delta_j + \cos\delta_j \cdot n_{Au} + i\frac{n_{Au}}{\eta_{bPAs}}\sin\delta_j + i\eta_{bPAs}\sin\delta_j} \right|^2$$

where $\delta_j = \frac{2\pi}{\lambda}(\eta_{bPAs} d_{bPAs})$, η_{bPAs} is complex refractive index of bPAs, d_{bPAs} is thickness of bPAs, n_{Au} is complex refractive index of Au.[37]

The measured data are fitted with the R equation above with least-squares method. Complete reconstruction of experimental data using fitted (n, k) values can be found in the Supporting Information.

Cavity Fabrication. A Si wafer evaporated with 100 nm Au and sputtered with 180 nm Al_2O_3 is used for the exfoliation substrate of bPAs. Thickness of bPAs is measured with atomic force microscope (AFM, Dimension Icon with ScanAsyst from Bruker). Separately, h-BN (purchased from hQ graphene) is exfoliated with Scotch tape and transferred to Si wafers using PDMS. ITO is sputtered on top of h-BN, where the thickness of h-BN is measured with AFM. Poly(methyl methacrylate) (PMMA) dry transfer is used for transferring h-BN-ITO to bPAs. In brief, PMMA is transferred on top of h-BN-ITO, annealed at 180 °C for 90 s, picked up and transferred on top of target bPAs, annealed at 180 °C for 3 min, and finally dissolved in dichloromethane (DCM).

ASSOCIATED CONTENT

Supporting Information

The Supporting Information is available free of charge at https://pubs.acs.org/doi/10.1021/acsnano.3c12927.

BPAs composition from SEM-EDS; polarized Raman spectra for bPAs (alloys); reconstructed anisotropic reflection of bPAs alloys with different thicknesses on Au from fitted (n,k) values; thickness and power dependence of PLspectra for bPAs alloys; TEM crystal structure analysis of bPAs alloys; low temperature PL spectra for bPAs (alloys) (PDF)

AUTHOR INFORMATION

Corresponding Author

Ali Javey − *Materials Sciences Division, Lawrence Berkeley National Laboratory, Berkeley, California 94720, United States; Berkeley Sensor & Actuator Center and Electrical Engineering and Computer Sciences, University of California, Berkeley, California 94720, United States;* orcid.org/0000-0001-7214-7931; Email: ajavey@berkeley.edu

Authors

Shu Wang − *Department of Materials Science and Engineering and Berkeley Sensor & Actuator Center, University of California, Berkeley, California 94720, United States; Materials Sciences Division, Lawrence Berkeley National Laboratory, Berkeley, California 94720, United States;* orcid.org/0000-0001-8812-817X

Naoki Higashitarumizu − *Materials Sciences Division, Lawrence Berkeley National Laboratory, Berkeley, California 94720, United States; Berkeley Sensor & Actuator Center and Electrical Engineering and Computer Sciences, University of California, Berkeley, California 94720, United States;* orcid.org/0000-0003-3996-6753

Bengisu Sari − *Department of Materials Science and Engineering, University of California, Berkeley, California 94720, United States; Materials Sciences Division, Lawrence Berkeley National Laboratory, Berkeley, California 94720, United States; The National Center for Electron Microscopy, Molecular Foundry, Berkeley, California 94720, United States;* orcid.org/0000-0002-4421-7098

Mary C. Scott − *Department of Materials Science and Engineering, University of California, Berkeley, California 94720, United States; Materials Sciences Division, Lawrence Berkeley National Laboratory, Berkeley, California 94720, United States; The National Center for Electron Microscopy, Molecular Foundry, Berkeley, California 94720, United States*

Complete contact information is available at: https://pubs.acs.org/10.1021/acsnano.3c12927

Notes

The authors declare no competing financial interest.

ACKNOWLEDGMENTS

This work was supported by the U.S. Department of Energy, Office of Science, Office of Basic Energy Sciences, Materials Sciences and Engineering Division under contract No.DE-AC02-05-CH11231 (EMAT program KC1201).

REFERENCES

(1) Haug, A. Auger Recombination in Direct-Gap Semiconductors: Band-Structure Effects. *J. Phys. C Solid State Phys.* **1983**, *16* (21), 4159−4172.

(2) Ling, X.; Wang, H.; Huang, S.; Xia, F.; Dresselhaus, M. S. The Renaissance of Black Phosphorus. *Proc. Natl. Acad. Sci. U. S. A.* **2015**, *112* (15), 4523−4530.

(3) Bhaskar, P.; Achtstein, A. W.; Vermeulen, M. J. W.; Siebbeles, L. D. A. Radiatively Dominated Charge Carrier Recombination in Black Phosphorus. *J. Phys. Chem. C* **2016**, *120* (25), 13836−13842.

(4) Narita, S.; Terada, S.; Mori, S.; Muro, K.; Akahama, Y.; Endo, S. Far-Infrared Cyclotron Resonance Absorptions in Black Phosphorus Single Crystals. *J. Phys. Soc. Jpn.* **1983**, *52* (10), 3544−3553.

(5) Morita, A. Semiconducting Black Phosphorus. *Appl. Phys. Solids Surf.* **1986**, *39* (4), 227−242.

(6) Kim, H.; Uddin, S. Z.; Lien, D.-H.; Yeh, M.; Azar, N. S.; Balendhran, S.; Kim, T.; Gupta, N.; Rho, Y.; Grigoropoulos, C. P.; Crozier, K. B.; Javey, A. Actively Variable-Spectrum Optoelectronics with Black Phosphorus. *Nature* **2021**, *596* (7871), 232−237.

(7) Huang, S.; Zhang, G.; Fan, F.; Song, C.; Wang, F.; Xing, Q.; Wang, C.; Wu, H.; Yan, H. Strain-Tunable van Der Waals Interactions in Few-Layer Black Phosphorus. *Nat. Commun.* **2019**, *10* (1), 2447.

(8) Chen, X.; Lu, X.; Deng, B.; Sinai, O.; Shao, Y.; Li, C.; Yuan, S.; Tran, V.; Watanabe, K.; Taniguchi, T.; Naveh, D.; Yang, L.; Xia, F. Widely Tunable Black Phosphorus Mid-Infrared Photodetector. *Nat. Commun.* **2017**, *8* (1), 1672.

(9) Huang, S.; Lu, Y.; Wang, F.; Lei, Y.; Song, C.; Zhang, J.; Xing, Q.; Wang, C.; Xie, Y.; Mu, L.; Zhang, G.; Yan, H.; Chen, B.; Yan, H. Layer-Dependent Pressure Effect on the Electronic Structure of 2D Black Phosphorus. *Phys. Rev. Lett.* **2021**, *127* (18), No. 186401.

(10) Amani, M.; Regan, E.; Bullock, J.; Ahn, G. H.; Javey, A. Mid-Wave Infrared Photoconductors Based on Black Phosphorus-Arsenic Alloys. *ACS Nano* **2017**, *11* (11), 11724−11731.

(11) Long, M.; Gao, A.; Wang, P.; Xia, H.; Ott, C.; Pan, C.; Fu, Y.; Liu, E.; Chen, X.; Lu, W.; Nilges, T.; Xu, J.; Wang, X.; Hu, W.; Miao, F. Room Temperature High-Detectivity Mid-Infrared Photodetectors Based on Black Arsenic Phosphorus. *Sci. Adv.* **2017**, *3* (6), No. e1700589.

(12) Usman, M.; Nisar, S.; Kim, D.; Golovynskyi, S.; Imran, M.; Dastgeer, G.; Wang, L. Polarization-Sensitive Photodetection of

Anisotropic 2D Black Arsenic. *J. Phys. Chem. C* **2023**, *127* (19), 9076−9082.
(13) Chang, T.-Y.; Chen, P.-L.; Chen, P.-S.; Li, W.-Q.; Li, J.-X.; He, M.-Y.; Chao, J.-T.; Ho, C.-H.; Liu, C.-H. Van Der Waals Heterostructure Photodetectors with Bias-Selectable Infrared Photoresponses. *ACS Appl. Mater. Interfaces* **2022**, *14* (28), 32665−32674.
(14) Chen, P.-L.; Chang, T.-Y.; Chen, P.-S.; Chan, A. H.-Y.; Rosyadi, A. S.; Lin, Y.-J.; Huang, P.-Y.; Li, J.-X.; Li, W.-Q.; Hsu, C.-J.; Na, N.; Lee, Y.-C.; Ho, C.-H.; Liu, C.-H. Van Der Waals Heterostructure Mid-Infrared Emitters with Electrically Controllable Polarization States and Spectral Characteristics. *ACS Nano* **2023**, *17* (11), 10181−10190.
(15) Zhang, J.; Xie, M.; Zhang, Y.; Wang, J.; Zhao, X.; Chen, C.; Zhang, Q.; Xia, M.; Li, J.; Dong, Z.; Zhang, Y.; Ren, Z.; Liu, T.; Pan, A.; Wang, S.; Zhang, K. Wide-Wavelength Tunable Mid-Infrared Lasing Based on Black Arsenic Phosphorus. *Adv. Opt. Mater.* **2023**, *11* (14), No. 2300278.
(16) Liu, B.; Köpf, M.; Abbas, A. N.; Wang, X.; Guo, Q.; Jia, Y.; Xia, F.; Weihrich, R.; Bachhuber, F.; Pielnhofer, F.; Wang, H.; Dhall, R.; Cronin, S. B.; Ge, M.; Fang, X.; Nilges, T.; Zhou, C. Black Arsenic−Phosphorus: Layered Anisotropic Infrared Semiconductors with Highly Tunable Compositions and Properties. *Adv. Mater.* **2015**, *27* (30), 4423−4429.
(17) Higashitarumizu, N.; Uddin, S. Z.; Weinberg, D.; Azar, N. S.; Reaz Rahman, I. K. M.; Wang, V.; Crozier, K. B.; Rabani, E.; Javey, A. Anomalous Thickness Dependence of Photoluminescence Quantum Yield in Black Phosphorous. *Nat. Nanotechnol.* **2023**, *18* (5), 507−513.
(18) Gupta, N.; Kim, H.; Azar, N. S.; Uddin, S. Z.; Lien, D.-H.; Crozier, K. B.; Javey, A. Bright Mid-Wave Infrared Resonant-Cavity Light-Emitting Diodes Based on Black Phosphorus. *Nano Lett.* **2022**, *22* (3), 1294−1301.
(19) *NIST Standard Reference Database 69: NIST Chemistry WebBook*. https://webbook.nist.gov/cgi/cbook.cgi?ID=C124389&Type=IR-SPEC&Index=1 (accessed 2024-01-16).
(20) Izquierdo, N.; Myers, J. C.; Golani, P.; De Los Santos, A.; Seaton, N. C. A.; Koester, S. J.; Campbell, S. A. Growth of Black Arsenic Phosphorus Thin Films and Its Application for Field-Effect Transistors. *Nanotechnology* **2021**, *32* (32), 325601.
(21) Wang, Y.; Chen, C.; Tang, Z.; Lu, H.; Cao, S.; Zhang, W.; Yi, M.; Zhang, K.; Liu, Y.; Guo, W. Tunable Bandgap of Black Phosphorus by Arsenic Substitution toward High-Performance Photodetector. *Sci. China Mater.* **2023**, *66* (6), 2364−2371.
(22) Zhong, M.; Xia, Q.; Pan, L.; Liu, Y.; Chen, Y.; Deng, H.; Li, J.; Wei, Z. Thickness-Dependent Carrier Transport Characteristics of a New 2D Elemental Semiconductor: Black Arsenic. *Adv. Funct. Mater.* **2018**, *28* (43), No. 1802581.
(23) Antonatos, N.; Mazánek, V.; Lazar, P.; Sturala, J.; Sofer, Z. Acetonitrile-Assisted Exfoliation of Layered Grey and Black Arsenic: Contrasting Properties. *Nanoscale Adv.* **2020**, *2* (3), 1282−1289.
(24) Chen, Y.; Chen, C.; Kealhofer, R.; Liu, H.; Yuan, Z.; Jiang, L.; Suh, J.; Park, J.; Ko, C.; Choe, H. S.; Avila, J.; Zhong, M.; Wei, Z.; Li, J.; Li, S.; Gao, H.; Liu, Y.; Analytis, J.; Xia, Q.; Asensio, M. C.; Wu, J. Black Arsenic: A Layered Semiconductor with Extreme In-Plane Anisotropy. *Adv. Mater.* **2018**, *30* (30), No. 1800754.
(25) Brown, A.; Rundqvist, S. Refinement of the Crystal Structure of Black Phosphorus. *Acta Crystallogr.* **1965**, *19* (4), 684−685.
(26) Dobrowolski, J. A.. Optical Properties of Films and Coatings. In *Handbook of optics*; McGraw-Hill, 1995; Vol. *1*, p 42.10−42.12.
(27) Bullock, J.; Amani, M.; Cho, J.; Chen, Y.-Z.; Ahn, G. H.; Adinolfi, V.; Shrestha, V. R.; Gao, Y.; Crozier, K. B.; Chueh, Y.-L.; Javey, A. Polarization-Resolved Black Phosphorus/Molybdenum Disulfide Mid-Wave Infrared Photodiodes with High Detectivity at Room Temperature. *Nat. Photonics* **2018**, *12* (10), 601−607.
(28) Crosby, G. A.; Demas, J. N. Measurement of Photoluminescence Quantum Yields. *Review. J. Phys. Chem.* **1971**, *75* (8), 991−1024.
(29) Shen, X.; Peterson, J. C.; Guyot-Sionnest, P. Mid-Infrared HgTe Colloidal Quantum Dot LEDs. *ACS Nano* **2022**, *16* (5), 7301−7308.
(30) *Hamamatsu Products*. https://www.hamamatsu.com/us/en/product/light-and-radiation-sources/led.html (accessed 2024-01-17).
(31) *Roithner Lasertechnik Product*. https://roithner-laser.com/led_midir_standard.html (accessed 2024-01-17).
(32) Varshni, Y. P. Temperature Dependence of the Energy Gap in Semiconductors. *Physica* **1967**, *34* (1), 149−154.
(33) Warschauer, D. Electrical and Optical Properties of Crystalline Black Phosphorus. *J. Appl. Phys.* **1963**, *34* (7), 1853−1860.
(34) Villegas, C. E. P.; Rocha, A. R.; Marini, A. Anomalous Temperature Dependence of the Band Gap in Black Phosphorus. *Nano Lett.* **2016**, *16* (8), 5095−5101.
(35) Huang, S.; Wang, F.; Zhang, G.; Song, C.; Lei, Y.; Xing, Q.; Wang, C.; Zhang, Y.; Zhang, J.; Xie, Y.; Mu, L.; Cong, C.; Huang, M.; Yan, H. From Anomalous to Normal: Temperature Dependence of the Band Gap in Two-Dimensional Black Phosphorus. *Phys. Rev. Lett.* **2020**, *125* (15), No. 156802.
(36) Zhang, Y.; Wang, S.; Chen, S.; Zhang, Q.; Wang, X.; Zhu, X.; Zhang, X.; Xu, X.; Yang, T.; He, M.; Yang, X.; Li, Z.; Chen, X.; Wu, M.; Lu, Y.; Ma, R.; Lu, W.; Pan, A. Wavelength-Tunable Mid-Infrared Lasing from Black Phosphorus Nanosheets. *Adv. Mater.* **2020**, *32* (17), No. 1808319.
(37) Olmon, R. L.; Slovick, B.; Johnson, T. W.; Shelton, D.; Oh, S.-H.; Boreman, G. D.; Raschke, M. B. Optical Dielectric Function of Gold. *Phys. Rev. B* **2012**, *86* (23), No. 235147.

https://doi.org/10.1021/acsnano.3c12927
ACS Nano 2024, 18, 5907−5914